JCTC Journal of Chemical Theory and Computation

Article

pubs.acs.org/JCTC

Comparison of Molecular Dynamics with Classical Density Functional and Poisson−Boltzmann Theories of the Electric Double Layer in Nanochannels

Jonathan W. Lee, Robert H. Nilson, Jeremy A. Templeton,* Stewart K. Griffiths, Andy Kung, and Bryan M. Wong

Sandia National Laboratories, Livermore, California, United States

ABSTRACT: Comparisons are made among Molecular Dynamics (MD), Classical Density Functional Theory (c-DFT), and Poisson−Boltzmann (PB) modeling of the electric double layer (EDL) for the nonprimitive three component model (3CM) in which the two ion species and solvent molecules are all of finite size. Unlike previous comparisons between c-DFT and Monte Carlo (MC), the present 3CM incorporates Lennard-Jones interactions rather than hard-sphere and hard-wall repulsions. c-DFT and MD results are compared over normalized surface charges ranging from 0.2 to 1.75 and bulk ion concentrations from 10 mM to 1 M. Agreement between the two, assessed by electric surface potential and ion density profiles, is found to be quite good. Wall potentials predicted by PB begin to depart significantly from c-DFT and MD for charge densities exceeding 0.3. Successive layers are observed to charge in a sequential manner such that the solvent becomes fully excluded from each layer before the onset of the next layer. Ultimately, this layer filling phenomenon results in fluid structures, Debye lengths, and electric surface potentials vastly different from the classical PB predictions.

INTRODUCTION

The structure of the electric double layer (EDL) on a charged surface has long been modeled using the Poisson−Boltzmann (PB) theory. PB incorporates Coulombic interactions among charged particles but treats them as point charges, neglecting their finite size. Although this omission is relatively unimportant at low charge densities, it permits physically unrealistic ion packing densities when the surface potential and charge density become large, as occurs for example in energy storage applications.[1] To treat this deficiency, a number of modified PB theories have been devised over the years[2] and have met with some success, though they lack the fundamental foundation needed to accommodate a broad range of molecular interactions.

Molecular dynamics (MD) simulation provides the most fundamental and flexible platform for analysis of molecular interactions. As such, it has been used rather extensively in modeling of electro-osmotic flow (EOF)[3−8] and to treat the higher charge densities of importance in EDL capacitors.[9−11] However, MD simulations entail considerable computational cost, making them impractical for treatment of time and length scales found in many applications. Difficulties also arise in applying boundary conditions and in computing long-range Coulombic interactions. For these reasons, alternative methods are still sought.

Alternative methods include modified PB approaches, integral equation methods, and classical Density Functional Theory (c-DFT). c-DFT, sometimes referred to as fluids DFT, yields the time-mean density distributions of molecular species that minimize a free energy functional.[12−17] The free energy at any point is defined by a density weighted integration of molecular pair potentials over the surroundings. Thus, c-DFT and MD are readily comparable given the same pair potentials and input parameters. Unlike MD, however, c-DFT readily incorporates long-range Coulombic interactions as the product of ion charge with the electric potential obtained by solving Poisson's equation. In addition, the c-DFT formalism yields an expression for the chemical potential in terms of pair-potential integrals over the surrounding field. This chemical potential can be incorporated into existing finite element models of steady and transient transport processes, thus facilitating the introduction of atomistic physics into efficient multiscale models. Finally, c-DFT computing times are far shorter than those required for MD.

Validation of c-DFT for EDL applications has been ongoing for the past 20 years; it has encompassed a broad range of variants on the basic methodology and has been largely quite successful.[13,14,16,17] However, these past validations are largely limited to comparisons between c-DFT and Monte Carlo (MC) simulations for the so-called primitive model (PM), in which the ions have defined charge and finite size but the solvent is treated as a background continuum defined only by its dielectric constant. Two exceptions to this are the studies by Goel et al.[18,19] and Lamperski and Zydor,[20] which compare c-DFT with MC for a nonprimitive three component model (3CM), in which the solvent and ions are all treated as distinct molecular species differing in charge and size. However, all of these comparisons with MC simulations treat the ions as hard spheres and the charged surface as a hard wall.

Unlike those previous studies, the present paper compares c-DFT with MD results for the 3CM. In further contrast with prior work, 12−6 Lennard-Jones interactions among all species are included, and the wall interaction is modeled by the one-dimensional Lennard-Jones 10−4−3 potential, as these are more realistic and more compatible with MD practice than hard

Received: February 8, 2012
Published: May 1, 2012

interactions. In addition, the present comparisons are extended to considerably greater charge densities than previously explored, reaching into a range relevant to energy storage.

We view these increases in complexity and range of the EDL model as a first step toward validation of c-DFT in a more realistic setting. This step is in the direction of the more general MD studies of EOF[3−8] which also include the additional complexity of polar solvents, atomistically structured walls, and cross-flow. An added complication for EOF is the apparent enhanced visocity within the EDL.[8] In our earlier effort to model EOF,[21] we achieved favorable velocity-profile comparisons with MD simulation[4] by assuming a uniform viscosity, and even better results when applying the modified Chapman−Enskog model for density-dependent viscosity.[22] Comparison with MD results is also hindered by the absence of knowledge regarding a reference state or chemical potential that is typically needed for comparison with c-DFT. In order to directly extract that information, the reference state (adjoining reservoir or bulk fluid in this case) must be explicitly modeled. Otherwise, those properties must be inferred via other means, such as the Widom insertion method for the chemical potential.[23] In addition, previous MD simulations of the EDL[3−8,10,24−27] have generally dealt with large ion concentrations and low surface charge densities, hence narrow EDLs with a single dominant "Stern layer" peak more nearly consistent with PB theory. In the current work, MD simulations were performed for a large range of ion concentrations and for surface charge densities many times greater than is typical of EOF. In most cases, the bulk region can be clearly distinguished, thereby revealing the reference state needed for comparison with c-DFT.

For the results of this paper, agreement between c-DFT and MD is deemed excellent, though it degrades somewhat with increasing charge density. The following three sections describe the details for PB, c-DFT simulations, and MD simulations. This is followed by a discussion of the results and concluding remarks.

PB THEORY

Here, we provide an overview of the classical PB theory. While it is understood that modified PB theories exist and provide improved model predictions,[28] we choose to compare specifically with the classical standard since it is still in widespread use. Moreover, the classical result provides model validation for a specific regime, which will be discussed in more detail later in the paper.

In the PB formulation, ions near the wall form according to the Boltzmann distribution. The first order approximation for the electrolytes is expressed as

$$n_+ = n_+^o \exp\left(\frac{-\phi e}{k_B T}\right) \text{ and } n_- = n_-^o \exp\left(\frac{\phi e}{k_B T}\right) \tag{1}$$

n is the concentration of the ion species, the superscript o denotes the bulk value, ϕ is the local value of the total electric potential (relative to the bulk value), e is the elemental charge value, k_B is the Boltzmann constant, and T is the temperature. The summation of the two densities is the volume density of ionic charge, ρ. For a 1:1 electrolyte, i.e., $n^o = n_+^o = n_-^o$, ρ is then given by

$$\begin{aligned}\rho(\phi) &= n^o e\left[\exp\left(\frac{-\phi e}{k_B T}\right) - \exp\left(\frac{\phi e}{k_B T}\right)\right] \\ &= -2n^o e \sinh\left(\frac{\phi e}{k_B T}\right)\end{aligned} \tag{2}$$

The 1D Poisson equation[29] is

$$\frac{d^2\phi}{dz^2} = \frac{2n^o e}{\varepsilon}\sinh\left(\frac{\phi e}{k_B T}\right) \tag{3}$$

Multiplying both sides by $2(d\phi/dz)$ gives

$$\frac{d}{dz}\left(\frac{d\phi}{dz}\right)^2 = \frac{4n^o e}{\varepsilon}\sinh\left(\frac{\phi e}{k_B T}\right)\frac{d\phi}{dz} \tag{4}$$

Integrating both sides from a point with zero potential (i.e., in the bulk) to some point at a finite potential (i.e., in the double layer, $z > d$) yields

$$\begin{aligned}\int_{\phi'=0}^{\phi'=\phi(z)} \mathrm{d}\left(\frac{d\phi'}{dz}\right)^2 &= \int_{\phi'=0}^{\phi'=\phi(z)} \frac{4n^o e}{\varepsilon} \sinh\left(\frac{\phi' e}{k_B T}\right)\mathrm{d}\phi' \\ \left(\left.\frac{d\phi'}{dz}\right|_{\phi'=\phi(z)}\right)^2 - \left(\left.\frac{d\phi'}{dz}\right|_{\phi'=0}\right)^2 &= \frac{4n^o k_B T}{\varepsilon} \cosh\left(\frac{\phi' e}{k_B T}\right)\Bigg|_{\phi'=0}^{\phi'=\phi(z)}\end{aligned} \tag{5}$$

Following the application of the Neumann boundary condition for the bulk, the result becomes

$$\frac{d\phi(z)}{dz} = -\frac{2\kappa k_B T}{e}\sinh\left(\frac{\phi(z)e}{2k_B T}\right) \tag{6}$$

where $\kappa \equiv (2n^o e^2/\varepsilon k_B T)^{1/2}$ is the inverse Debye length. After a separation of variables, a second integration from the wall to a point in the double layer ultimately leads to

$$\phi(z) = \frac{4k_B T}{e}\tanh^{-1}\left(\tanh\left(\frac{\phi_w e}{4k_B T}\right)\exp[-\kappa(z-d)]\right) \tag{7}$$

where ϕ_w is the total electric potential evaluated at the wall−fluid interface. Inserting eq 7 back into the ionic charge density equation, eq 2, yields the charge density as a function of position. Integrating the ionic charge density over all space yields the applied surface charge density.

C-DFT SIMULATIONS

In c-DFT, the equilibrium density distributions, $\rho_i(\mathbf{r})$, of multiple molecular species are determined by minimizing the grand potential energy, Ω, of the system,[12−17]

$$\Omega[\{\rho\}] = \sum_i \int \rho_i(\mathbf{r})\,(f_i(\mathbf{r}) - \mu_i)\,\mathrm{d}\mathbf{r} \tag{8}$$

Here, $f_i(\mathbf{r})$ is the Helmholtz free energy per molecule of the ith species, μ_i is the corresponding chemical potential, and the integral extends over the three-dimensional domain of interest. The curly braces on ρ denote the set of unknown equilibrium

dx.doi.org/10.1021/ct3001156 | J. Chem. Theory Comput. 2012, 8, 2012−2022

density distributions. Here, we utilize a version of c-DFT developed at the University of Minnesota by Davis and colleagues.[12−14] In particular, our EDL calculations will utilize the 3CM in which the two ion species are represented as centrally charged spheres and the solvent molecules are treated as neutral spheres.[14,18,20] Electrostatic interactions arising from the solvent molecules are represented by the dielectric constant of the solvent, presumed to be spatially uniform.

The free energy consists of contributions from ideal gas behavior, the external potential field, $v(\mathbf{r})$, excess hard sphere repulsions, Lennard-Jones attractions,[30] Coulombic forces, and short-range electrostatic interactions evaluated using the Mean Spherical Approximation (MSA) of Waisman and Lebowitz:[31,32]

$$f_i(\mathbf{r}, \{\rho\}) = f_i^{\mathrm{ig}} + v(\mathbf{r}) + f_i^{\mathrm{hs}} + \frac{1}{2}(f_i^{\mathrm{LJ}} + f_i^{\mathrm{Coul}} + f_i^{\mathrm{MSA}}) \tag{9}$$

The ideal gas component depends on the local species density, temperature, de Broglie wavelength, Λ_i, and Boltzmann's constant:

$$f_i^{\mathrm{ig}}(\rho_i(\mathbf{r})) = k_{\mathrm{B}}T[\ln(\Lambda_i^3\rho_i(\mathbf{r})) - 1] \tag{10}$$

The external field, $v(\mathbf{r})$, is the nonelectrical portion of the potential field induced by the solid walls. In most of the calculations presented here, $v(\mathbf{r})$ is obtained by integration of a Lennard-Jones potential over planar sheets of wall atoms. The integration[33] leads to the LJ 10−4−3 potential of the form:

$$v(z) = 2\pi\varepsilon^{\mathrm{LJ}}\left[\frac{2}{5}\left(\frac{d}{z}\right)^{10} - \left(\frac{d}{z}\right)^{4} - \frac{\sqrt{2}\,d^3}{3(z + (0.61/\sqrt{2})d)^3}\right] \tag{11}$$

where d is the LJ diameter and z is the wall-normal position measured from the wall. Note that the potential is a one-dimensional potential and is therefore a function of z, and not the general position, $\mathbf{r}$. The potential is cut off outside of 3.5 molecular diameters and shifted by subtracting the value at the cutoff.

Hard sphere exclusions of liquid molecules, modeled by f_i^{hs}, are included to avoid integration of self-interactions. The excess free energy is based on the following formula derived from the Carnahan−Starling equation of state:

$$f_i^{\mathrm{hs}}(\overline{\rho}(\mathbf{r})) = k_{\mathrm{B}}T\eta\frac{4 - 3\eta}{(1 - \eta)^2}, \quad \eta = \overline{\rho}\frac{\pi d_{\mathrm{hs}}^3}{6} \tag{12}$$

The normalized mean density, η, appearing here represents the volume fraction occupied by molecules having a hard sphere diameter d_{hs}. The local mean density, $\overline{\rho}(\mathbf{r})$, used in calculating these repulsions is a weighted average over the surrounding fluid:

$$\overline{\rho}(\mathbf{r}) = \int[\omega^0(s) + \omega^1(s)\,\overline{\rho}(\mathbf{r}) + \omega^2(s)\,\overline{\rho}^2(\mathbf{r})]\,\rho(\mathbf{r}')\,\mathrm{d}\mathbf{r}' \tag{13}$$

The weight functions, $\omega^k(s)$, are chosen in accordance with a third-order scheme derived by Tarazona;[34] a corrected version is given by Vanderlick et al.[12] The weighting functions are prescribed as

$$\omega^0(s) \equiv \begin{cases} \dfrac{3}{4\pi d^3}, & s < d \\ 0, & s > d \end{cases} \tag{14a}$$

$$\omega^1(s) \equiv \begin{cases} 0.475 - 0.648\left(\dfrac{s}{d}\right) + 0.113\left(\dfrac{s}{d}\right)^2, & s < d \\ 0.288\left(\dfrac{d}{s}\right) - 0.924 + 0.764\left(\dfrac{s}{d}\right) - 0.187\left(\dfrac{s}{d}\right)^2, & d < s < 2d \\ 0, & s > 2d \end{cases} \tag{14b}$$

$$\omega^2(s) \equiv \begin{cases} \dfrac{5\pi d^3}{144}\left[6 - 12\left(\dfrac{s}{d}\right) + 5\left(\dfrac{s}{d}\right)^2\right], & s < d \\ 0, & s > d \end{cases} \tag{14c}$$

where $s = |\mathbf{r} - \mathbf{r}'|$ is the relative atomic position. Here, we will assume that all molecular species have the same diameter, d_{hs}, thus permitting the local summation of all species into the total densities, $\rho(\mathbf{r})$, used in computing $\overline{\rho}(\mathbf{r})$.

Attractive energies are defined by a density weighted integral of a pair potential function, $U_{ij}(s)$, over the surrounding fluid, separately summing the contributions from each species:

$$f_i^{\mathrm{LJ}}(\mathbf{r}, \{\rho\}) = \sum_j \int \rho_j(\mathbf{r}')\,U_{ij}(s)\,\mathrm{d}\mathbf{r}' \tag{15}$$

Although the LJ 12−6 potential is used in nearly all c-DFT modeling, authors differ in how they extract the attractive part. We follow one common approach by splitting the potential at its crossover point, $s = d$, and cutting it off at $s = s_{\max} = 3.5d$.

$$U_{ij}(s) = 4\varepsilon_{ij}^{\mathrm{LJ}}\left[\left(\frac{d}{s}\right)^{12} - \left(\frac{d}{s}\right)^{6}\right] \quad \text{for } d \le s \le s_{\max} \tag{16}$$

Outside this interval, $U = 0$. To avoid a slight discontinuity in U_{ij} at $s = s_{\max}$, this truncated function is shifted by subtracting $U_{ij}(s_{\max})$.

Coulombic contributions to the free energy are computed as the product of the molecular charge, $q_i = ez_i$, with the local electric potential, ϕ:

$$f_i^{\mathrm{Coul}}(\mathbf{r}) = q_i\phi(\mathbf{r}) \tag{17}$$

The electric potential field is obtained by solving Poisson's equation,[29]

$$\nabla^2\phi = -\frac{4\pi}{\varepsilon}\sum_{i=1}^{N} z_i e\rho_i \tag{18}$$

in which ε is the permittivity of the liquid, e is the elementary charge, and z_i is the number of charges per molecule.

The free energy associated with short-range electrostatic interactions is modeled using MSA[31,32]

$$f_i^{\mathrm{MSA}}(\mathbf{r}, \{\rho\}) = \sum_j \int \rho_j(\mathbf{r}')\,\Delta c_{ij}(\mathbf{r} - \mathbf{r}')\,\mathrm{d}\mathbf{r}' \tag{19}$$

$$\Delta c_{ij} = \frac{q_i q_j}{\varepsilon}\left[\frac{2B}{d} - \left(\frac{B}{d}\right)^2 s - \frac{1}{s}\right], \quad s < d \tag{20}$$

$$B = \frac{d^* + 1 - \sqrt{1 + 2d^*}}{d^*}, \quad d^* = d/\lambda \tag{21}$$

$$\lambda = \left[\frac{4\pi}{\varepsilon k_B T}\sum_i \rho_i q_i^2\right]^{-1/2} \tag{22}$$

Here, λ is the Debye length which we evaluate using local values of the species densities in the manner suggested by Gillespie et al.[15] and Wang et al.,[16] rather than using the reference densities that refer to the bulk reservoir fluid, as was done in most early implementations of MSA.[13,14] The diameter appearing here is taken as the exclusion diameter, d_{hs}.

By taking the variation of Ω with respect to $\rho_i(\mathbf{r})$, we obtain the following expression for the chemical potential of each species, applicable to all points, $\mathbf{r}$:

$$k_B T \ln \rho_i + v_i + f_i^{LJ} + f_i^{Coul} + f_i^{MSA} + f_i^{hs} + f_i^{hs2} = \mu_i \tag{23}$$

The new term, f_i^{hs2}, arises from (Fréchet) functional differentiation of the nonlinear hard sphere repulsion term:

$$f_i^{hs2}(\mathbf{r}, \{\rho\}) = \int \bar{\rho}(\mathbf{r}) \frac{\partial f_i^{hs}}{\partial \rho_i}(\mathbf{r}')\, d\mathbf{r}' \tag{24}$$

Numerical solutions to the preceding integral equations are obtained on a discrete grid having a uniform spacing of $d/30$. All of the integrals appearing in the c-DFT equations are represented as weighted summations over the surrounding grid points. The weight factors in these summations are calculated by numerical quadrature prior to numerical solution, and these weights remain fixed unless the grid is redefined. Moreover, in the case of 1D c-DFT, integration over two of the three dimensions can be performed at the onset to obtain weights describing interactions between slabs of volume bounded by parallel planes defined by their distance from the planar electrode surfaces. Introduction of this discretization into eq 23 then yields an independent equation for each species density at each grid point. This system of nonlinear algebraic equations is then solved iteratively to obtain the equilibrium density field. For a 1-D system with a channel width of $w = 10d$, iterative solutions to the resulting system of coupled nonlinear equations require about a minute of computing time on a single 3 GHz Dual-Core Intel Xeon CPU processor to obtain five digit accuracy after 4000 iterations. The numerical quadratures and primitive iteration scheme are detailed in ref 34.

MD SIMULATIONS

MD simulations of a similar electrically charged nanochannel were performed with the LAMMPS software package.[35] Important to note is that the MD domain is sufficiently wide in the wall-normal direction so that the bulk fluid can be explicitly modeled to measure ion molarities, solvent density, and the electric potential. The simulation domain consists of the electrolyte fluid bounded in the z dimension by LJ 10−4−3 walls, as discussed previously, and in the transverse directions with periodic boundary conditions. Transverse dimensions are 5 nm × 5 nm, and the longitudinal dimension varies depending on the bulk ion concentration. Interatomic potentials were modeled with the superposition of a typical LJ 12−6 potential with Coulomb's law, both with a 1.3 nm cutoff. The pairwise potential is an abrupt cutoff, contrary to c-DFT, which is cut and shifted. Fluid−wall interactions are treated as described in the c-DFT section.

Equations of motion were integrated with the velocity-Verlet algorithm[36,37] and a timestep of 0.0005 ps. The electrolyte fluid is comprised of positive, negative, and neutral LJ atoms, all with the same interaction parameters. The atoms are assigned a mass of 18.0154 g per mole. To account for the dielectric effects of a polar solvent, the dielectric constant ε_r was set to 80 to approximate water.[3,5] In general, polar solvent molecules will solvate ionic charges and prevent oppositely charged ions from approaching too closely. This can be mimicked by reducing all Coulombic interactions by the value of the dielectric constant. Long range Coulombics are computed using the PPPM algorithm[38] with slab geometry.[39]

To facilitate equilibration, the initial system contains only uncharged particles. The number of particles must be selected such that the final steady state configuration produces the correct bulk concentrations and densities. Note that this procedure requires some iteration to target the desired values, and it can be approximately informed by the steady state configuration from the c-DFT calculations or PB theory. The atom velocities are all initialized to zero since potential energy variations will cause the system kinetic energy to increase rapidly. This uncharged system is equilibrated to 300 K for 100 000 timesteps using the Nosé−Hoover[40−42] thermostat. Following the initial equilibration, fluid particles are randomly selected and assigned positive or negative electric charges. The selection process fills each approximate EDL region with counterions and randomly assigns the rest of the ions to the remainder of the domain according to a uniform distribution. This produces a biased overall distribution aimed to expedite equilibration. A background electric field is applied to simulate equally and oppositely charged surfaces. The charged system is then equilibrated for 500 000 more timesteps to 300 K. To avoid any local minima in the energy landscape, the system is annealed to 1000 K for 500 000 timesteps, followed by a cooling step back to 300 K for 1 million timesteps.

Following equilibration, thermostats are turned off. The system is allowed to evolve toward a steady state solution for 5 million timesteps. The first 1 million timesteps are treated as transient, and the remaining timesteps are confirmed to be statistically steady. Five permutations of this simulation are performed for each molarity and surface charge combination. The permutations differ in the initial configuration of atom positions. To increase sampling in the larger domain for 10 mM, an additional five permutations are simulated, and each production run is shortened by 1 million timesteps. Not all molarity and surface charge combinations are tested due to computational difficulty in achieving good statistics for low ion counts and low surface charges.

Spatial dependent particle concentrations are extracted by species from the domain via an atomistic-to-continuum (AtC) interpolation method.[43] The resolution of the 1-D continuum mesh is approximately 0.1 Å. Density data are sampled every 0.25 ps. After removing the transient data, the remaining data are time- and ensemble-averaged. Species concentrations, scaled by the atomic charge, yield the spatially resolved free charge density, ρ_{free}. Integrating Poisson's equation

$$\nabla\cdot(\varepsilon_0\varepsilon_r\mathbf{E}) = \rho_{\text{free}} \tag{25}$$

produces the z component of the electric field. Note that, consistent with c-DFT, ε_r = 80 is assumed to be pervasive in this integration, regardless of the presence or absence of solvent. Furthermore, the electric field is offset by the applied field, which is also augmented by the relative permittivity. The electric potential can similarly be obtained by integrating the electric field:

$$-\nabla\phi = \mathbf{E} \tag{26}$$

The bare wall potential, also known as the electric surface potential, is determined by taking the electric potential at the fluid−wall contact point in reference to the electric potential evaluated in the bulk; see Figure 1. For this study, the contact

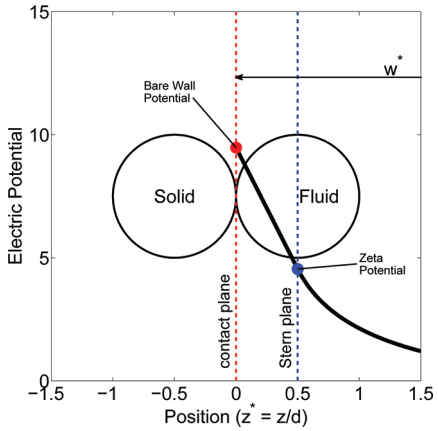

Figure 1. Diagram of zeta potential (blue) and bare wall potential (red), also known as the electric surface potential. Since finite atom sizes are foreign to PB theory, it makes no distinction between the two. The diagram also shows where the channel width, w^*, is measured from.

plane, not to be confused with the shear plane where the zeta potential is measured, is defined to be one-half a molecular diameter away from the LJ 10−4−3 origin, to be consistent with the c-DFT calculation. Moving the measurement location within the free space region will merely add a linear offset to the electric potential (linear with respect to the applied surface charge) since the amount of charge does not change. The ion molarities are also measured by taking the average density of the channel center.

RESULTS

Results are reported in terms of normalized position, $z^* = z/d$, channel width $w^* = w/d$, density $\rho^* = \rho d^3$, potential $\phi^* = \phi e/k_BT$, and surface charge $\sigma^* = \sigma d^2/e$. Parameters used in the EDL simulations are given in Table 1.

Bulk ion densities are varied from 1 mM to 1 M. The lower end of this range is typical of microscale chemical laboratory devices, while the upper end applies to electrochemical energy storage devices and desalination processes. Within this range of ion concentrations, the Debye thickness from PB theory λ decreases from approximately 97 to 3 Å or, equivalently, λ/d decreases from 30 to 1 with increasing concentration. Thus, to avoid excessive EDL overlap, we utilized a channel width of w^* = 12.55 for bulk concentrations of 100 mM and 1 M, but increased the width to w^* = 100 for the 10 mM and 1 mM runs. Note that these bulk ion concentrations refer to the state

Table 1. Simulation Parameters for c-DFT and MD Calculations[a]

parameter	c-DFT	MD
atom−atom ε^{LJ} (eV)	0.006596	0.006596
atom−atom d (Å)	3.1507	3.1507
atom−atom inner cutoff (Å)	2.9302	N/A
atom−atom outer cutoff (Å)	11.0275	13.0
atom−wall ε^{LJ} (eV)	0.1351	0.1351
atom−wall d (Å)	3.1507	3.1507
atom−wall outer cutoff (Å)	11.0275	11.0275
relative permittivity ε_r	80	80
nominal temperature (K)	300	300
atomic mass (g/mol)	N/A	18.0154

[a]The word "atom" is used to represent either a solvent or solute particle, as opposed to the LJ wall.

that would exist in a zero-potential reservoir of infinite extent in equilibrium with the charged channel. The same state would also be found at the center of a charged channel having a width much greater than the Debye thickness. For comparison purposes, the bulk of the MD domains is defined as the center ∼12 Å and ∼45 Å for the w^* = 12.55 and w^* = 100 channels, respectively, where the electric potential is observed to be relatively flat.

Channel widths quoted here represent the distance between the liquid/solid contact surfaces on opposite sides of the channels, as indicated in Figure 1. Similarly, the bare wall potentials reported here are measured at these same contact planes. Zeta potentials, by contrast, refer to the potential at the Stern plane: the center plane of the first layer of fluid molecules at a distance $d/2$ from the contact plane.

Preliminary Model Validation. Prior to the comparisons presented here, we had previously[21] used our c-DFT to replicate c-DFT results presented by Vanderlick et al.[12] and Tang et al.,[14] as well as two of the MD simulations presented by Magda et al.[33]

As a prelude to the upcoming comparisons of our MD and c-DFT for the EDL, we performed an initial comparison of density profiles for a fluid confined between uncharged planar walls. The parameters are taken from an MC simulation by Snook and van Megen[44] for a channel width of 7.5 measured between the center planes of the first layers of wall atoms in the 10−4−3 LJ walls; this is a width of 6.5 between fluid/solid contact planes. The LJ energies for the fluid−fluid and fluid−solid interactions are both taken as ε^{LJ}/k_BT = 0.833 and the chemical potential is μ/ε^{LJ} = −2.477, which corresponds to a bulk fluid having a normalized density of ρ^* = 0.5925. Since the authors reported the number of fluid molecules in their MC simulations, we used this to guide the number needed in our MD.

Figure 2 compares Snook's MC and our MD with our c-DFT results for two different choices of the hard sphere diameter. The c-DFT result for $d_{hs} = d_{LJ}$ (dotted lines) has a spacing between molecular layers slightly greater than that of the MD and the MC simulations. This mismatch is corrected by the use of $d_{hs} = 0.93d_{LJ}$ in the c-DFT calculation indicated by the solid line. This adjustment, similar in concept to the Barker−Henderson diameter,[45] helps to align the spacing while having negligible influence on the magnitude of the density peaks. Thus, we make this adjustment of spacing mainly to facilitate the upcoming comparisons between c-DFT and MD for the EDL.

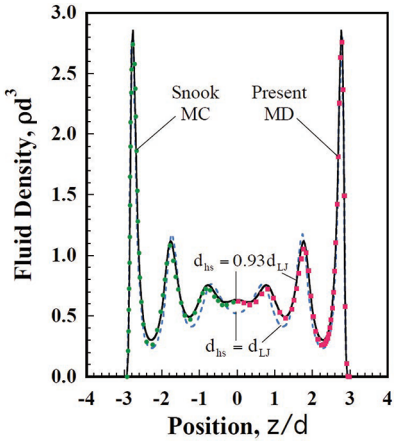

Figure 2. Snook MC (green circles) and present MD (red squares) compared to c-DFT (solid and dashed lines) with different choices of the hard sphere diameter, d_{hs}, relative to LJ diameter, d_{LJ}.

Comparison of c-DFT and MD Simulation of EDL. Figure 3 provides an overview comparison of computed surface

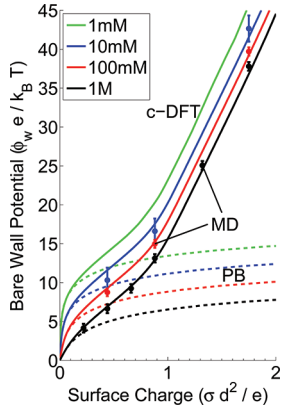

Figure 3. Capacitance comparison of three EDL models. MD is shown with circle markers and error bars which denote the standard deviation of the data set. c-DFT is shown with solid lines, and PB is shown with dashed lines. Colors denote bulk ion molarities, as shown in the legend.

potential versus surface charge density among our MD, our c-DFT, and classical PB modeling. This is a very important metric as the inverse slope of this plot is the capacitance. Since $k_BT/e \approx 25$ mV, the upper range of the potential slightly exceeds 1 V, typical of double layer capacitors.

MD results (symbols) are shown for three charge densities (0.44, 0.88, and 1.75) and for bulk concentrations of 10 mM, 100 mM, and 1 M. Additional charge densities (0.22, 0.66, 1.32) are included for 1 M. The agreement between MD and c-DFT is judged as excellent for 1 M but degrades moderately at the lower concentrations. MD results are not included for 1 mM due to the statistical difficulty in obtaining convergence of the very low ion densities in the channel center.

The classical PB results shown in Figure 3 are obtained by application of the Grahame equation,[46] which is strictly applicable only to a semi-infinite medium:

$$\sigma^{*2} = \frac{\rho_B^*}{\pi P}[\cosh(z\phi_w^*) - 1] \quad (27)$$

where $\rho_B^* = C_BAd^3$, C_BA is the bulk ion concentration in ions/Å^3 (molarity × Avogadro's number × 10^{-27}), and $P = e^2/4\pi\epsilon k_BTd$ is the plasma constant. Thus, the very precise agreement in electric surface potential between MD/c-DFT with PB at low charge density is an indication that our channel widths are sufficiently large to minimize the effects of EDL overlap. Also, such a precise agreement at low charges might not have been anticipated given that the layered density profiles of c-DFT and MD differ greatly from their smooth PB counterparts. Most importantly, it is seen that the PB substantially deviates from MD/c-DFT at charge densities of 0.5 or greater. In an effort to find a fairer comparison to the PB, we tried two alternatives. In the first of these attempts, we treated the bare wall potential of the PB as though it were a zeta potential and used the surface slope to extrapolate backward by $d/2$ to the corresponding bare wall location (see Figure 1). This produced a PB that rose much faster than the c-DFT/MD. As a second alternative, we compared the bare wall potential of the PB with the zeta potential of the c-DFT. This reduces the disparity between c-DFT/MD and PB at large surface charges since the zeta potential of the c-DFT/MD increases far more slowly than the bare wall potential, but such a comparison still involves substantial error.

Example concentration profiles for three charged cases are shown in Figures 4a, 5a, and 6a. All three examples are targeted to a 100 mM ion solution with varying surface charge loadings. Corresponding MD and c-DFT solutions are overlaid to show the agreement. Since populating the MD domain to a corresponding c-DFT case is a complex inverse problem, the MD models used as inputs integrated solvent and solute density

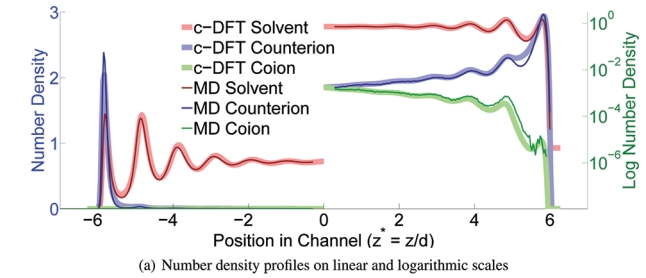

(a) Number density profiles on linear and logarithmic scales

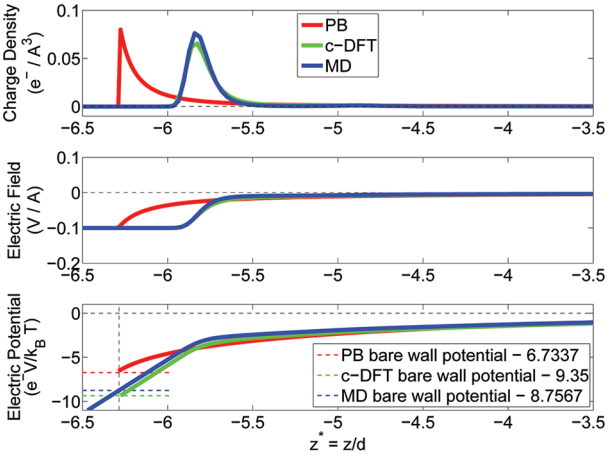

(b) Charge density, electric field, and electric potential comparison of MD/c-DFT/PB

Figure 4. MD/c-DFT EDL comparison for 0.44 normalized surface charge. Electryolyte concentration is 93.239 mM (100 mM target). Bulk solvent density, normalized by d^3, is 0.71711 (0.7 target).

dx.doi.org/10.1021/ct3001156 | J. Chem. Theory Comput. 2012, 8, 2012−2022

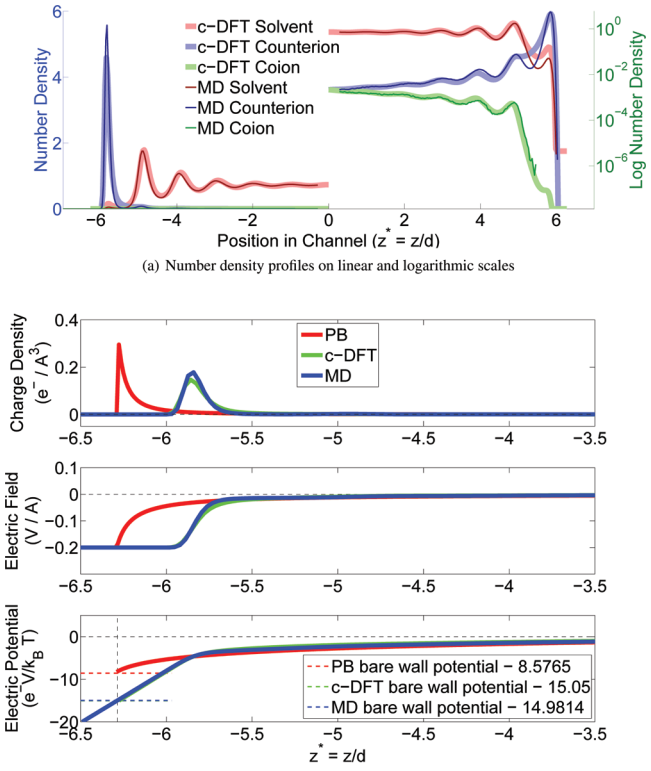

(a) Number density profiles on linear and logarithmic scales

(b) Charge density, electric field, and electric potential comparison of MD/c-DFT/PB

Figure 5. MD/c-DFT EDL comparison for 0.88 normalized surface charge. Electryolyte concentration is 113.45 mM (100 mM target). Bulk solvent density, normalized by d^3, is 0.72227 (0.7 target).

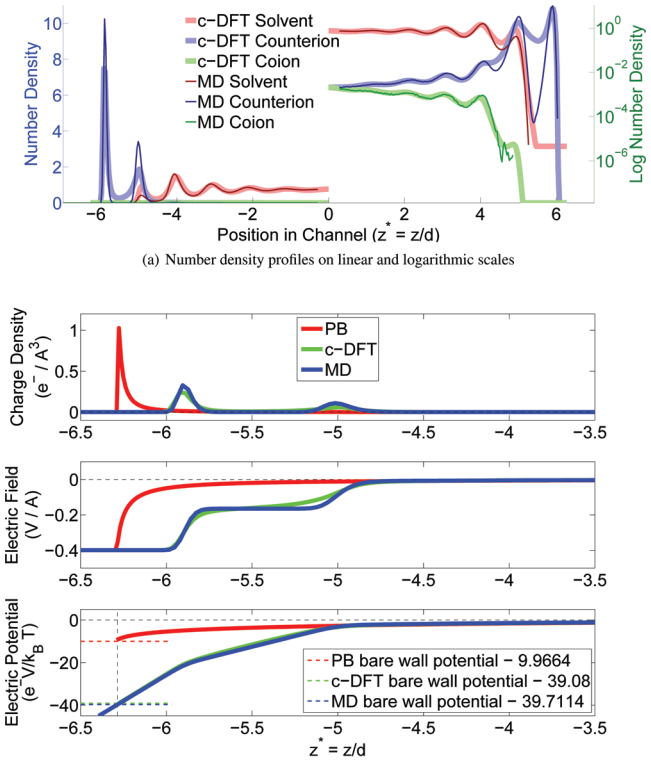

(a) Number density profiles on linear and logarithmic scales

(b) Charge density, electric field, and electric potential comparison of MD/c-DFT/PB

Figure 6. MD/c-DFT EDL comparison for 1.75 normalized surface charge. Electryolyte concentration is 107.59 mM (100 mM target). Bulk solvent density, normalized by d^3, is 0.74146 (0.7 target).

profiles and surface charge density outputs from the c-DFT simulations. Since agreement is good between the two models, this method produces nearly analogous cases for comparison. An additional c-DFT iteration to match the MD is also done in some cases. The left-hand sides of Figures 4a–6a show the concentration profiles on a linear scale, distinguished by atom types. The right sides of the figures are the analogous plots displayed on a logarithmic scale to showcase good agreement even over five to six decades.

The peak heights and widths appear to differ slightly between the two models, particularly near the wall. c-DFT tends to have broader, shorter peaks, while the MD has narrower, tall peaks. This is especially noticeable in the first two layers in Figure 6.

The particle density profiles are multiplied by the atom types' respective valences to obtain a charge density profile, which is shown in the top graph in Figures 4b, 5b, and 6b. The second and third plots correspond to the density profile once- and twice- integrated to obtain the z-component electric field and electric potential, respectively. The results from the two models are overlaid again in these plots, and the agreement is shown to be quite good. Even despite the slight mismatch in peak values observed in Figures 4a, 5a, and 6a, the integrals seem to converge to similar solutions. This is a result of having an equal amount of charge per layer, only differing in the mobility of the atoms within those layers.

Sequential Layer Charging Phenomenology. Charging of the EDL proceeds largely as a sequential layer-by-layer displacement of solvent molecules by counterions, as illustrated in Figure 7 with c-DFT results at 10 mM. Similar results were

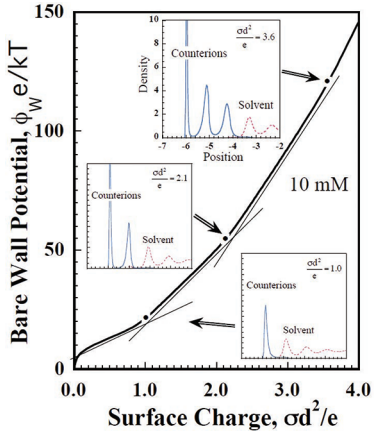

Figure 7. Layer filling phenomenology. Aside from initial nonlinear behavior, the capacitance trend is a nearly piecewise linear function. Inflection points correspond to solvent depletion from subsequent near-wall layers, as depicted in the figure insets.

observed in the MD, particularly at higher concentrations. As seen in the inset density profiles for $\sigma^* = 1.0$, all of the solvent has been displaced from the first layer prior to the formation of a second layer of counterions. With increasing surface charge density, the counterion density peaks in the first and second layers both continue to increase in height and narrow in width until all of the solvent has been excluded from the second layer, as seen in the inset for $\sigma^* = 2.1$. The third stage of the process continues in a similar fashion until all of the solvent has been displaced from the third layer at $\sigma^* = 3.6$.

Another interesting feature of this step-like layer filling process is that each stage proceeds with a nearly constant capacitance, as indicated by a constant slope in Figure 7. The

dx.doi.org/10.1021/ct3001156 | J. Chem. Theory Comput. 2012, 8, 2012–2022

transition from one stage to the next is smooth but most of the charging occurs as a piecewise linear process with the slope increasing (and the capacitance decreasing) with each successive stage. This seems physically reasonable, as it becomes more difficult to accumulate charge in layers more remote from the surface. However, this interpretation does not appear to apply in the initial charging of the first layer which begins with a very steep slope (small capacitance) before turning off onto a much flatter, nearly constant slope. The initial nonlinear phase occurs because ionic charges are relatively evenly distributed through the EDL for low surface charges. As loading increases, peak formation becomes energetically favorable, and most of the charge is found distributed near the walls, as shown in Figure 8. As the peak

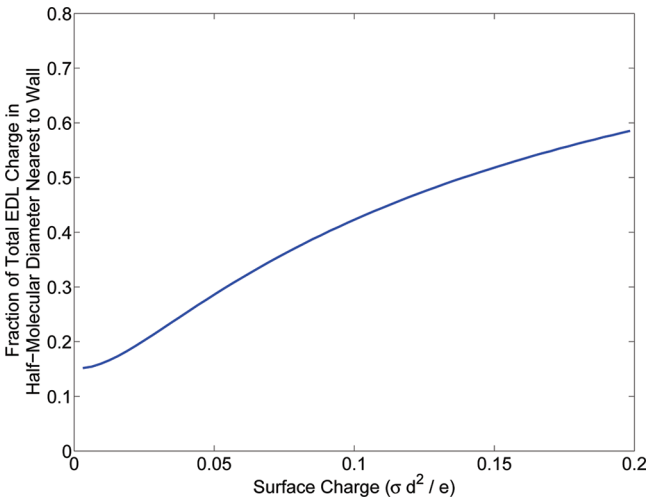

Figure 8. The distribution of charge in the EDL as surface charge increases (according to PB − similar trends are expected for MD and c-DFT since all three models are in good agreement in this regime). The fractional amount of charge found nearest the wall increases as surface charge increases. Prior to peak formation, the long tail of the EDL impacts the electric surface potential greatly, which causes the nonlinear charging trend.

builds up (likewise for subsequent layers), the peak structure's contributions begin to dominate those of the tail. Aside from the initial nonlinear phase, these features of the charging behavior are expressly absent from theories not accounting for finite size effects since the physics arise from layered density profiles and solvent displacement processes entirely foreign to PB.

MSA Treatments Leading to Charge Inversion. In MSA formulations of c-DFT, the Mean Spherical Approximation of Waisman and Lebowitz[31,32] is used to solve the Ornstein−Zernike equation relating the radial distribution functions and direct correlation functions of ion species. The resulting pair interactions can then be partitioned into a direct Coulombic contribution, a hard sphere repulsion, and an electric residual contribution with the latter given by our eqs 19−22.[16] Historically, the Debye length appearing in eq 19 had been evaluated using the ion concentrations of the bulk state existing within the center of a very wide channel or within an external reservoir, referred to here as the MSA_B approach. This was traditionally done, in part at least, to ensure electrical neutrality of the reference state since the MSA theory is derived as a perturbation about a neutral reference state. The expectation of the perturbation approximation is that the final result is a small correction to the reference. Given that large density variations occur near the walls, the perturbation ansatz can not be expected to work. More recent MSA implementations by Gillespie et al.[15] and Wang et al.[16] have used a local, nonuniform fluid as the reference state, as opposed to the bulk fluid. Because local ion concentrations are not electrically neutral, these authors defined an equivalent charge-neutral reference state having the same ionic strength as the local state. Thus, denoting reference densities with the subscript "ref," a pair of ion densities must satisfy the requirements that

$$\rho^+_{ref} + \rho^-_{ref} = \rho^+ + \rho^- \tag{28}$$

$$\rho^+_{ref}(q^+)^2 + \rho^-_{ref}(q^-)^2 = \rho^+(q^+)^2 + \rho^-(q^-)^2 \tag{29}$$

For the present univalent examples, the net result is that

$$\rho^+_{ref} = \rho^-_{ref} = (\rho^+ + \rho^-)^2 \tag{30}$$

Wang et al.[16] found this approach to be in good agreement with MC simulations[47] of a solvent primitive electrolyte. Here, we test this approach, referred to as MSA_L, against MD simulations of the 3CM in which ion and solvent species are all of finite size.

All of the preceding comparisons of c-DFT with MD use local ion densities evaluated at individual grid points to implement MSA_L. We find that those comparisons with MD are moderately degraded when the "local" Debye length is computed in an alternative manner by averaging over a surrounding sphere of molecular size, as suggested in previous versions of MSA_L.[31,32] But these differences are very minor compared to deviations between MSA_L and MSA_B versions of c-DFT. As seen in Figure 9a, the ion concentrations in the first layer do not differ greatly in using these different versions of MSA, but the MSA_L produces a broader spreading of non-neutral ion concentrations into the central region of the channel. This leads to a substantial difference in the electric potential distributions depicted in Figure 9b. The MSA_L profile has a much broader region of gradually changing slope, resulting in a surface potential about 20% greater than MSA_B. Also included in Figure 9b is a c-DFT calculation that entirely excludes the MSA electric residual terms while retaining the Coulombic and hard sphere interactions, referred to as MSA_0. This leads to a surface potential that is about 20% above MSA_L. Given the excellent agreement of MSA_L with MD in our earlier results, we conclude that MSA_B and MSA_0 should be rejected in favor of MSA_L.

Differences between MSA_L and MSA_B are further illustrated in Figure 10 which displays bare wall and zeta potentials. The potentials for MSA_B (solid lines) generally fall below the corresponding results for MSA_L (dotted lines). This can be seen by comparing the MSA_B and MSA_L results for 1 mM, which are both indicated in Figure 10 in green and by comparing Figure 10 with Figure 3. Another interesting feature of Figure 10 is that the zeta potential for MSA_B becomes negative for bulk concentrations of 1 M and for charges ranging from 0.4 to 0.9. This is an indication of overscreening or charge inversion which occurs when counterions adjacent to the electrode are more than sufficient to screen the surface charge. Although this phenomenon has been seen in some previous MD simulations (with polar solvent),[4,6] it does not occur in our MD (with nonpolar solvent) or MSA_L predictions for the parameter ranges considered here. So it is suspected that the charge inversion seen in Figure 10 may be an incorrect c-DFT

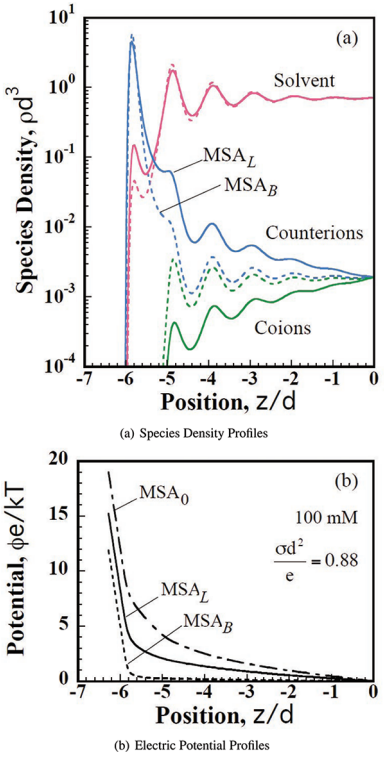

Figure 9. Comparison of results obtained with alternative implementation of MSA. Local evaluation of Debye length in MSA$_L$ produces broader distribution of counterions and higher surface potentials than bulk evaluation in MSA$_B$. MSA$_L$ is in best agreement with MD results, as suggested by comparisons in Figures 3−6.

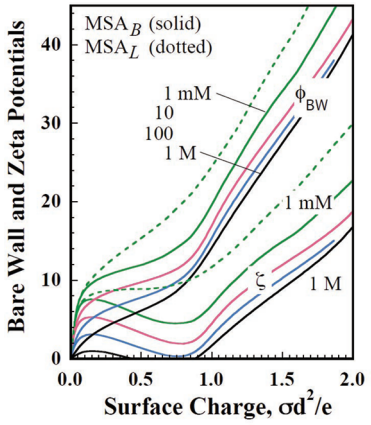

Figure 10. Capacitance comparison for MSA$_B$ (solid lines) vs MSA$_L$ (dashed lines). The bare wall potentials are the upper curves, labeled as ϕ_{BW}, and the zeta potentials are the lower curves, labeled as ζ. Colors denote bulk ion molarities, as indicated in the plot. MSA$_B$ predicts strong charge inversion and negative zeta potentials for 1 M, in contrast to MSA$_L$ and MD.

result that arises from the MSA$_B$ approximation. To better understand this phenomenon, we are studying the effects of polar solvents in an ongoing research.

Charge inversion attributed to MSA$_B$ is also illustrated in Figure 11. Here, the solid symbols indicate the MC results of Lamperski and Zydor[20] for a 3CM similar to the present 3CM except that the molecules are hard spheres and the electrode surface is a hard wall; there are no LJ interactions. Also, the bulk density is 0.573 rather than 0.7, and the problem is posed

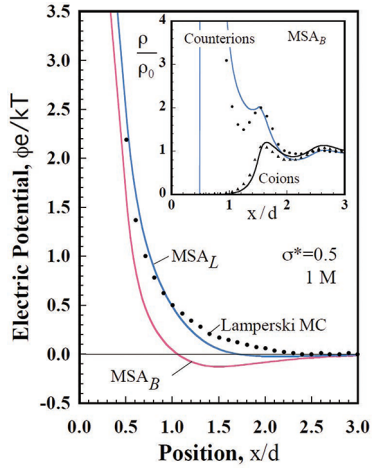

Figure 11. MSA$_B$ and MSA$_L$ implementation schemes compared with Lamperski MC electric potential and ion density profiles. MSA$_B$ produces charge inversion in contrast to MSA$_L$ and MC.

on a semi-infinite domain. Our MSA$_L$ results for this configuration are in reasonably good agreement with Lamperski's MC, whereas our MSA$_B$ results indicate charge inversion and a resulting region of significant opposite potential near the electrode. The charge inversion is reversed in regions farther from the electrode where the coions outnumber the counterions, as apparent in the inset of Figure 11.

Figure 12 compares the zeta and bare wall potentials computed by Lamperski (symbols) with our MSA$_L$ and MSA$_B$

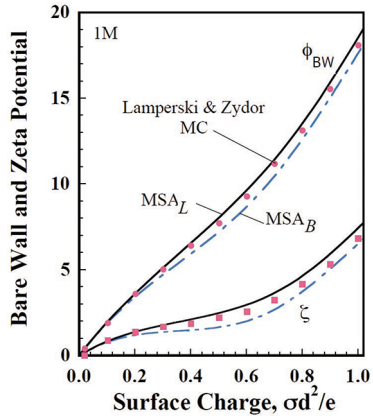

Figure 12. Bare wall and zeta potential trends of MSA$_B$ and MSA$_L$ implementation schemes compared with Lamperski's MC.

results. It is seen here that the two versions of c-DFT tightly bracket the MC results. So, from this comparison, there is no reason to prefer one approach over the other. We note that differences between our c-DFT MSA$_L$ and Lamperski's MC results, particularly those in the potential profiles of Figure 11, may arise partly from differing treatments of electrostatic interactions. The MC uses the method of charged planes to estimate long-range forces, which is thought to be less accurate[24] than the corrected 3D Ewald summations used in our MD and the Poisson solver used in our c-DFT.

CONCLUSION

MD and c-DFT models of electrolyte fluids contained within nanochannels were studied and compared to classical PB

dx.doi.org/10.1021/ct3001156 | J. Chem. Theory Comput. 2012, 8, 2012−2022

theory. To facilitate proper comparison, special care was taken to model analogous parameters with both techniques. The simulations performed in this study used the 3CM, in which solvent and solute are represented by three distinct molecular species. The fluid−fluid and fluid−solid interactions use LJ-type potentials, in contrast to previous c-DFT-to-MC comparison studies, which utilized hard-sphere and hard-wall repulsions. In further contrast with previous studies, our simulations cover a wide range of electrolyte concentrations and surface charge densities. Our MD models are able to simulate concentrations as low as 10 mM and still produce density profiles in agreement with c-DFT over a five to six decade range. All of our nanochannels are sufficiently wide to prevent overlapping EDLs, even in the case of low ion concentrations (hence large Debye lengths). A discernible bulk region with zero potential is important for direct comparison between MD and c-DFT.

As a result, MD and c-DFT methods are in excellent agreement for various qualitative and quantitative assessments, particularly for large molarities. Metrics for assessment include atomic density, charge density, electric field, and electric potential profiles, as well as capacitance trends for various loadings and concentrations. Specifically, density profiles agreed particularly well on peak location and spacing, while differing slightly on peak height and width. Comparisons are improved when c-DFT uses a modified hard sphere radius of $d_{hs} = 0.93d_{LJ}$ and the MSA_L implementation. MD calculations tended to have taller, narrower peaks than the c-DFT; this is resolved by the fact that there is an equivalent amount of charge in the layer.

Moreover, as electrolyte concentration decreases and surface charge loading increases, deviation from PB becomes increasingly apparent. These trends highlight the effect of distinct ion packing layers, which is due to the finite sizes of electrolyte and solute. Distinct layers result in significantly reduced capacitances relative to the predictions from PB theory. Further investigation shows a layer packing phenomenon in which a new ion peak begins to form when solvent is completely expelled from the previous fluid layer. The onset of the new ion peak produces a kink in the electric field and electric potential profiles, thereby reducing the capacitance of the EDL. Since this behavior arises from finite size effects, it is not captured in PB theory.

This work is a step toward modeling more complex systems. As mentioned previously, we will be exploring complex EOF models with polar solvents and atomistically structured walls including surface roughness. We are exploring the plausibility of modeling structured walls with higher dimensional c-DFT to study surface effects such as packing structures. Additionally, by modeling representative unit cells with 3D c-DFT and linking them with a continuum-like boundary conditions, we can study large-scale surface roughness.

AUTHOR INFORMATION

Corresponding Author

*E-mail: jatempl@sandia.gov.

Notes

The authors declare no competing financial interest.

ACKNOWLEDGMENTS

Funding for this effort was provided by the Laboratory Directed Research and Development (LDRD) program at Sandia National Laboratories, a multiprogram laboratory operated by Sandia Corporation, a Lockheed Martin Company, for the United States Department of Energy's National Nuclear Security Administration under contract DE-AC04-94AL85000.

REFERENCES

(1) Conway, B. E. *Electrochemical Supercapacitors*; Kulwer Academic: New York, 1999.
(2) Wang, H.; Laurent, P. *J. Phys. Chem. C* **2011**, *115*, 16711−16719.
(3) Freund, J. B. *J. Chem. Phys.* **2002**, *116*, 2194−2200.
(4) Qiao, R.; Aluru, N. R. *J. Chem. Phys.* **2003**, *118*, 4692−4701.
(5) Thompson, A. P. *J. Chem. Phys.* **2003**, *119*, 7503−7511.
(6) Qiao, R.; Aluru, N. R. *Phys. Rev. Lett.* **2004**, *92*, 198301.
(7) Kim, D.; Darve, E. *Phys. Rev. E* **2006**, *73*, 051203.
(8) Wu, P.; Qiao, R. *Phys. Fluids* **2011**, *23*, 072005.
(9) Cui, S. T.; Cochran, H. D. *J. Chem. Phys.* **2002**, *117*, 5850−5854.
(10) Feng, G.; Qiao, R.; Huang, J.; Sumpter, B. G.; Meunier, V. *ACS Nano* **2010**, *4*, 2382−2390.
(11) Wander, M. C. F.; Shuford, K. L. *J. Phys. Chem. C* **2010**, *114*, 20539−20546.
(12) Vanderlick, T. K.; Scriven, L. E.; Davis, H. T. *J. Chem. Phys.* **1989**, *90*, 2422−2436.
(13) Tang, Z. X.; Mier-y-Teran, L.; Davis, H. T.; Scriven, L. E.; White, H. S. *Mol. Phys.* **1990**, *71*, 369−392.
(14) Tang, Z.; Scriven, L. E.; Davis, H. T. *J. Chem. Phys.* **1992**, *97*, 494−503.
(15) Gillespie, D.; Nonner, W.; Eisenberg, R. S. *Phys. Rev. E* **2003**, 68.
(16) Wang, Z.; Liu, L.; Neretnieks, I. *J. Phys.: Condens. Matter* **2011**, 23.
(17) Patra, C. N.; Ghosh, S. K. *J. Chem. Phys.* **2002**, *117*, 8938−8943.
(18) Goel, T.; Patra, C. N.; Ghosh, S. K.; Mukherjee, T. *J. Chem. Phys.* **2008**, 129.
(19) Goel, T.; Patra, C. N.; Ghosh, S. K.; Mukherjee, T. *J. Phys. Chem. B* **2011**, *115*, 10903−10910.
(20) Lamperski, S.; Zydor, A. *Electrochim. Acta* **2007**, *52*, 2429−2436.
(21) Nilson, R. H.,; Griffiths, S. K. *J. Chem. Phys.* **2006**, 125.
(22) Bitsanis, I.; Vanderlick, T. K.; Tirrell, M.; Davis, H. T. *J. Chem. Phys.* **1988**, *89*, 3152−3163.
(23) Widom, B. *J. Chem. Phys.* **1963**, *39*, 2808−2812.
(24) Crozier, P. S.; Rowley, R. L.; Spohr, E.; Henderson, D. *J. Chem. Phys.* **2000**, *112*, 9253−9257.
(25) Spohr, E. *Electrochim. Acta* **1999**, *44*, 1697−1705.
(26) Xu, D.; Li, D.; Leng, Y.; Chen, Y. *Mol. Simul.* **2007**, *33*, 959−963.
(27) Willard, A. P.; Reed, S. K.; Madden, P. A.; Chandler, D. *Faraday Discuss.* **2009**, *141*, 423−441.
(28) Lamperski, S.; Outhwaite, C. W.; Bhuiyan, L. B. *Mol. Phys.* **1996**, *87*, 1049−1061.
(29) Poisson, S. D. *Bull. Soc. Philomath. Paris* **1813**.
(30) Jones, J. E. *Proc. R. Soc. London, Ser. A* **1924**, *106*, 436−477.
(31) Waisman, E.; Lebowitz, J. L. *J. Chem. Phys.* **1972**, 56.
(32) Waisman, E.; Lebowitz, J. L. *J. Chem. Phys.* **1972**, 56.
(33) Magda, J. J.; Tirrell, M.; Davis, H. T. *J. Chem. Phys.* **1985**, *83*, 1888−1901.
(34) Tarazona, P. *Phys. Rev. A* **1985**, *31*, 2672−2679.
(35) Plimpton, S. J. *J. Comput. Phys.* **1995**, *117*, 1−19.
(36) Verlet, L. *Phys. Rev.* **1967**, *159*, 98−103.
(37) Verlet, L. *Phys. Rev.* **1968**, *165*, 201−214.
(38) Hockney, R. W.,; Eastwood, J. W. *Computer Simulation using Particles*; American Institute of Physics: New York, 1988.
(39) Yeh, I.-C.; Berkowitz, M. L. *J. Chem. Phys.* **1999**, *111*, 3155−3162.
(40) Nosé, S. *J. Chem. Phys.* **1984**, *81*, 511−519.
(41) Hoover, W. G. *Phys. Rev. A* **1985**, *31*, 1695−1697.
(42) Martyna, G. J.; Klein, M. L.; Tuckerman, M. *J. Chem. Phys.* **1992**, *97*, 2635−2643.
(43) Zimmerman, J. A.; Webb, E. B., III; Hoyt, J. J.; Jones, R. E.; Klein, P. A.; Bammann, D. J. *Modell. Simul. Mater. Sci. Eng.* **2004**, *12*, S319−S332.
(44) Snook, I.; van Megen, W. *J. Chem. Phys.* **1979**, *70*, 3099−3105.

(45) Barker, J. A.; Henderson, D. *J. Chem. Phys.* **1967**, *47*, 4714−4721.
(46) Grahame, D. C. *Chem. Rev.* **1947**, *41*, 441−501.
(47) Torrie, G. M.; Valleau, J. P. *Chem. Phys. Lett.* **1979**, *65*, 343−346.